

See discussions, stats, and author profiles for this publication at: <https://www.researchgate.net/publication/6933141>

# Charge Separation in Heterostructures of InP Nanocrystals with Metal Particles

ARTICLE in THE JOURNAL OF PHYSICAL CHEMISTRY B · NOVEMBER 2005

Impact Factor: 3.3 · DOI: 10.1021/jp051201y · Source: PubMed

CITATIONS

7

READS

18

6 AUTHORS, INCLUDING:



**Nada M Dimitrijevic**

Argonne National Laboratory

125 PUBLICATIONS 4,259 CITATIONS

SEE PROFILE



**Tijana Rajh**

Argonne National Laboratory

176 PUBLICATIONS 7,501 CITATIONS

SEE PROFILE



**Jovan M Nedeljković**

Vinča Institute of Nuclear Sciences

188 PUBLICATIONS 3,494 CITATIONS

SEE PROFILE



**A. J. Nozik**

University of Colorado Boulder

310 PUBLICATIONS 19,419 CITATIONS

SEE PROFILE

# Charge Separation in Heterostructures of InP Nanocrystals with Metal Particles

Nada M. Dimitrijević and Tijana Rajh

Chemistry Division, Argonne National Laboratory, 9700 South Cass Avenue, Argonne, Illinois 60439

S. Phillip Ahrenkiel, Jovan M. Nedeljković, Olga I. Mičić,\* and Arthur J. Nozik

National Renewable Energy Laboratory, 1617 Cole Boulevard, Golden, Colorado 80401

Received: March 8, 2005; In Final Form: July 27, 2005

The optical and electron paramagnetic resonance (EPR) properties of InP nanocrystals, in which metallic gold or indium is present as an incorporated part of the nanocrystals, have been studied. A study of Au/InP quantum rods supports different carrier localization regimes compared to metal-free quantum rods, including the charge-separated state for which the electron and hole are located in different parts of the heterostructure. They also show that elongated semiconductors that grow on metallic catalysts have electronic properties that are different from those of pure semiconductor nanocrystals of the same shape. We have also developed a simple method for growing melted indium particles on the surface of colloidal spherical InP nanocrystals, and in these In/InP nanocrystals the emission is completely quenched while the absorption spectrum moves to red due to the strong mixing of the semiconductor and metal electronic states.

## Introduction

Photogenerated electrons confined to nanometer-size regions of a semiconductor have been the subject of intensive studies. Various properties of semiconductor quantum dots (QDs) and quantum rods (QRs) can be altered by bringing them in contact with different materials. An insulator shell provides a well-defined potential barrier that confines the electron and hole inside nanocrystals with a large excitonic binding energy that, for example, for 4.2-nm InP QDs is 120 meV.<sup>1</sup> The exciton binding energy in QRs is even larger due to dielectric enhancement caused by the difference between the dielectric constant of the semiconductor nanocrystal and the surrounding medium.<sup>2,3</sup> The electron and hole are at a distance larger than the QR radius and interact predominantly through the surrounding medium, which has a smaller dielectric constant. This leads to the formation of one-dimensional excitons with a large binding energy.<sup>2</sup> For InP quantum wires with a 3.8-nm diameter, the exciton binding energy is about 190 meV with a dielectric constant 2 for the surrounding medium.<sup>2</sup> If the difference of the dielectric constant of the constituent parts of the QRs is varied, it is possible to change the binding energy of the excitons. The presence of a metal on the nanocrystals can produce this effect and also increase delocalization of electrons inside the nanocrystals; this lowers the confinement energy compared to core QDs with no metal. With recent advances in techniques for synthesizing different semiconductor and metallic nanocrystals, it is now possible to synthesize quantum structures with a metal nanoparticle incorporated onto or into the semiconductor nanocrystal.

Most synthetic methods for growing elongated nanocrystals in solution use a colloidal metallic catalyst to initiate the growth process. The growth process proceeds via a solution–liquid–solid (SLS)<sup>4</sup> or a vapor–liquid–solid (VLS) mechanism,<sup>5</sup> and the final product contains metallic catalyst particles on the wire

tip. Liquid metallic droplets (Au or In) have been widely used in the SLS method as the catalyst to synthesize wirelike crystallites of zinc blende cubic-lattice semiconductors (InAs, InP, and GaAs) with controllable diameters and excellent crystallinity.<sup>6–8</sup> However, the presence of metal as an incorporated part of the semiconductor nanostructure can be expected to change the optical and electronic properties of the nanocrystals. Their electronic states are a mixture of the semiconductor and metal electronic states.

For semiconductor nanocrystals with large band gap (ZnO, TiO<sub>2</sub>),<sup>9,10</sup> the presence of metal on their surface promotes interfacial charge-transfer kinetics between the semiconductor and metal and improves the charge separation. For semiconductor nanocrystals that are in the strong confinement regime, there are only a few published studies of the effect of the metal on the electronic properties of the semiconductor. It has been found that luminescence enhancement of CdSe QDs near a nanostructured gold surface occurs when the spacing between the QD and gold is in the range of a few nanometers due to the locally enhanced electromagnetic field produced by the gold nanoparticles.<sup>11,12</sup> However, when the distance between the gold particle and the QD is further decreased and results in intimate contact, quenching of the emission occurs. Very recently, Banin et al.<sup>13</sup> showed that the growth of gold tips on CdSe QRs with different gold sizes was caused by a strong coupling between the gold and the CdSe parts. In that case, the emission is quenched by the metal tips via nonradiative pathways created by the proximity of the metal. The different electronic properties of semiconductor–metal nanocrystals compared to those of pure semiconductor nanocrystals create the advantage of having better charge separation inside the nanocrystals and formation of metal anchor points, which can serve as a contact for wiring nanocrystals onto an electrical circuitry. However, there are no available data in the literature that show whether charge separation occurs and where the photoinduced electron and hole are located in the semiconductor quantum structure when metal nanoparticles are incorporated.

\* Author to whom correspondence should be addressed. E-mail: Olga\_Micic@nrel.gov.

We report here on the studies of the optical and electron paramagnetic resonance (EPR) properties of InP nanocrystals in which metallic gold or indium is present as an incorporated component. The combination of metal and semiconductor provides new functionalities to the nanostructures and the possibility of charge separation. InP QRs are so far produced using gold as the growth catalyst, and hence the understanding of the contribution of the metal component in charge separation processes is investigated in InP–Au QRs. EPR investigation of charge separation in InP–In QRs was not feasible due to the extremely large hyperfine coupling of In that would lead to weak EPR signals. Our experiments studying paramagnetic species with the EPR techniques show that charge separation occurs in Au/InP quantum rods and that the electron is located in the metal particle while the hole remains in the interface between the InP rod and Au particle. EPR measurements also show that elongated semiconductors that grow on metallic catalysts have different electronic properties compared to pure nanocrystals of the same shape. For spherical semiconductor QDs, the presence of metal drastically interferes with the optical properties of the QDs. Growth of Au on InP nanoparticles was proved unsuccessful, and we developed a simple method for growing melted indium particles on the surface of colloidal spherical InP nanocrystals. We have shown that in In/InP nanocrystals the absorption spectrum moves to lower energy due to the strong mixing of the semiconductor and metal electronic states.

## Experimental Procedure

**1. Synthesis of Nanocrystals.** All compounds used in this work are extremely sensitive to oxygen and moisture, and they were manipulated in a Schlenk line or glovebox under rigorous air- and water-free conditions.

For preparation of In<sup>0</sup> nanoparticles, C<sub>5</sub>H<sub>5</sub>In is used; it spontaneously decomposes and yields indium particles. Indium particles of 8-nm diameter were synthesized by decomposition of 5–10 mg of C<sub>5</sub>H<sub>5</sub>In in 10 mL of toluene containing 0.1 mL of TOA in the absence of light at 50 °C.<sup>14</sup> The 160-Å In<sup>0</sup> particles were synthesized by decomposition of 100 mg of (CH<sub>3</sub>)<sub>5</sub>C<sub>5</sub>In in 56 mL of octadecene in the presence of 6.25 g of poly(1-hexadecene-*co*-vinylpyrrolidinone) (PHVP). The 2-nm thiol-derivatized gold nanoparticles were prepared using a two-phase liquid–liquid system described elsewhere.<sup>15</sup>

InP QRs without residual metallic catalysts were synthesized by reacting P(SiMe<sub>3</sub>)<sub>3</sub> with In<sup>0</sup> nanoparticles dispersed in organic solvent.<sup>14</sup> Short nanorods (6-nm diameter and 15-nm length) were prepared when a solution of 8-nm indium particles that contained 1 mg of In<sup>0</sup> were mixed with 30 mg of P(SiMe<sub>3</sub>)<sub>3</sub> in 2.5 mL of TOP, 2.5 mL of toluene, and 30 mg of hexadecylamine (HAD) and heated for 2 h at 110 °C in a closed system saturated with nitrogen. Larger rods (9-nm diameter and 66-nm length) were prepared by reaction of 1–3 mg of 16-nm indium particles with 20–30 mg of P(SiMe<sub>3</sub>)<sub>3</sub> in 2–4 mL of 1-octadecene overnight at 220 °C.

For the preparation of InP QRs in the presence of 2.0-nm Au catalyst, we used the procedure developed by Banin et al.<sup>6</sup> Briefly, a stock solution containing 85 mg of (SiMe<sub>3</sub>)<sub>3</sub>P, 1 mL of InCl<sub>3</sub>/TOP solution (0.15 g/mL), 0.5 mL of gold/toluene solution (6.7 mg/mL), and 0.5 mL of TOP was injected into the growth solution (2 g of TOPO) at 360 °C under vigorous stirring. Less than 3 s later, 2 g of cold TOP was injected to additionally quench the reaction temperature to 220 °C, and then the reaction mixture was cooled to room temperature. The precipitation with methyl alcohol followed with centrifugation was used to obtain fractions of QRs with different sizes.

We have prepared InP QDs capped with TOPO/TOP with a 4.8-nm diameter and a standard deviation of about 8%. Details of the nanocrystal synthesis may be found in ref 16. For the synthesis of the 3.5-nm InP quantum dots, the preparation described by Peng et al.<sup>17</sup> was followed with some changes. The difference is that we used oleic acid instead of the palmitic or myristic acid that was used by Peng et al. With oleic acid, we prepared highly fluorescent InP QDs with slightly broader size distribution (10%).

The metallic indium was deposited on the 3.5-nm InP QDs capped with oleate or 4.8-nm InP capped with TOPO/TOP by using spontaneous decomposition of C<sub>5</sub>H<sub>5</sub>In. Typically, 1 mg of the 3.5-nm InP QDs was dissolved in 3 mL of hexane that contains 10 mg of HDA, and 3 mg of C<sub>5</sub>H<sub>5</sub>In dissolved in 3 mL of hexane was added very slowly drop by drop over a period of 2 h by vigorously stirring at 40–50 °C in the glovebox. Then, the reaction mixture was cooled to room temperature. Optical changes of the In/InP QD composites were followed for two weeks. We found that pure InP QDs are formed when In<sup>0</sup>/InP particles are mixed with P(SiMe<sub>3</sub>)<sub>3</sub> in TOPO/TOP solution and heated at 260 °C for 2 h.

**2. Nanocrystals Characterization.** The EPR measurements were made at Argonne National Laboratory. X-band EPR experiments were collected on a Bruker ESP300E spectrometer equipped with a Varian rectangular cavity TE<sub>102</sub> and a variable temperature cryostat (Air Products) cooled to helium temperatures. Samples were excited either by a 300-W ILC xenon lamp with a 320-nm cutoff filter or, for higher radiant power (1–10 photons per particle), with a YAG-OPO laser (550-nm, and 10–20 mJ/pulse). The samples were kept under an argon atmosphere. Samples were excited directly in the EPR cavity at 4 K. Preliminary scans were obtained on the samples before irradiation to check for spurious signals. Temperature control for sample annealing was achieved with a Lake Shore 320 autotuning temperature controller. The sample was equilibrated for 20 min at the temperature before the spectrum was recorded at the temperature indicated on the figure. The *g*-factors were calibrated by comparison to Mn<sup>2+</sup> standard in SrO matrix (*g* = 2.0012 ± 0.0002)<sup>18</sup> and with a 1,1-diphenyl-2-picrylhydrazyl (DPPH) standard (*g* = 2.0036 ± 0.0003). A high concentration of particles (concentration of particles 10<sup>−5</sup> to 10<sup>−4</sup> M) was used in order to improve the quality of detection, as described previously.<sup>19</sup>

For microstructural analysis, colloidal samples were deposited on C-coated Cu grids. Characterization was carried out with a Philips CM200 STEM operated at 200 kV or a Philips CM30 TEM operated at 200 kV. For high-angle annular dark-field imaging, a JEOL JEM-2010F STEM operated at 200 kV was used. Bright-field and lattice images were acquired with an objective aperture that admitted contributions from low-index reflections. Selected-area patterns were acquired with an aperture having a projected diameter of approximately 7 μm in the image plane. EDX spectra were acquired with a Kevex Li-drifted Si detector using the Emispec ES Vision software. X-ray diffraction patterns were acquired on a Scintag ×1 diffractometer using Cu Kα radiation.

Optical absorption spectra were collected at room temperature using a Cary 5E UV–vis–NIR spectrophotometer. Steady-state photoluminescence spectra were collected at room temperature using a SPEX model 1691 fluorolog (excitation with a Xe lamp and cooled photomultiplier tube detector).

## Results and Discussion

**1. Paramagnetic Electron and Hole Species.** We have studied the paramagnetic species formed in illuminated hetero-

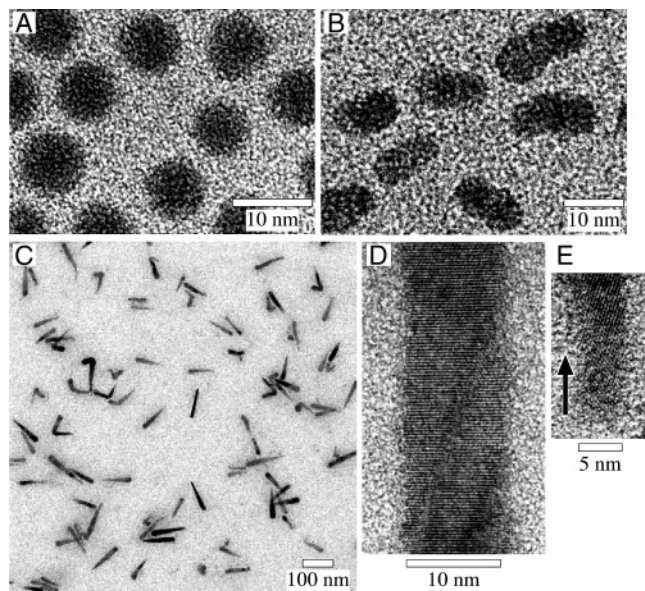


**Figure 1.** TEM images showing (a) In<sup>0</sup> nanoparticles, and (b–e) InP QRs. (b) QRs (6-nm diameter) with aspect ratios of 1.4–2.5 prepared from a solution of 8-nm In<sup>0</sup> particles at 110 °C. (c) QRs (9-nm diameter) with aspect ratio of 7 (tapered shape) prepared from a solution of 16-nm In<sup>0</sup> particles heated at 260 °C. (d, e) High-resolution images of the individual QRs.

structure Au/InP QRs that are synthesized by the SLS mechanism with gold nanoparticles as the catalyst. These results have been compared with those obtained for InP QRs that are metal-free and also for pure Au nanoparticles. With this analysis, we want to clarify the nature of the electron and the hole located in a QR in order to understand if charge separation occurs in Au/InP QRs. The nature of the paramagnetic species formed in Au nanoparticles is well-known,<sup>20</sup> and there are data in the literature showing their behavior in different matrixes.<sup>21</sup>

We first studied InP nanorods that do not contain gold particles and are catalyst-free. In this procedure, quantum rods were produced via the reactions of monodispersed colloidal indium droplets with P(SiMe<sub>3</sub>)<sub>3</sub> (the source of P<sup>3-</sup> ions) in organic solvent.<sup>14</sup> We prepared indium particles by thermal decomposition of C<sub>5</sub>H<sub>3</sub>In (Figure 1a). The dimension of the QRs depends on the dimension of the In<sup>0</sup> particles, the stabilizer used, and the temperature. Parts b and c of Figure 1 show InP nanorods prepared with trioctylphosphine/hexadecylamine (TOP/HDA) or hexadecene-*co*-vinylpyrrolidinone polymer (PHVP) stabilizers. Colloidal InP QRs having ~6-nm diameter and 15 nm-length with a TOP/HDA stabilizer were prepared from 8-nm In<sup>0</sup> droplets (Figure 1b), while QRs that have a 9-nm diameter and 60-nm length were prepared with PHVP from 16-nm In<sup>0</sup> droplets (Figure 1c). The PHVP polymer causes QRs to grow in one direction and to be straight, although the diameters changed during the growth process and the QRs have a tapered shape (Figure 1c). Both QRs have diameters that are significantly smaller than the corresponding bulk InP exciton Bohr diameter (20 nm). Rods with 9-nm diameter and 66-nm length have strong confinement only in the radial direction, while along the long axis they behave as bulk InP material.

In our previous work, we reported the observation of nonradiative and radiative paramagnetic species of spherical InP QDs by EPR<sup>22</sup> and by optically detected magnetic resonance (ODMR)<sup>23</sup> spectroscopy, respectively. Results obtained by EPR techniques for QDs and QRs are presented in Figure 2. When spherical nanocrystals were illuminated with a Xe lamp (Figure 2a) with a light intensity producing about one exciton per

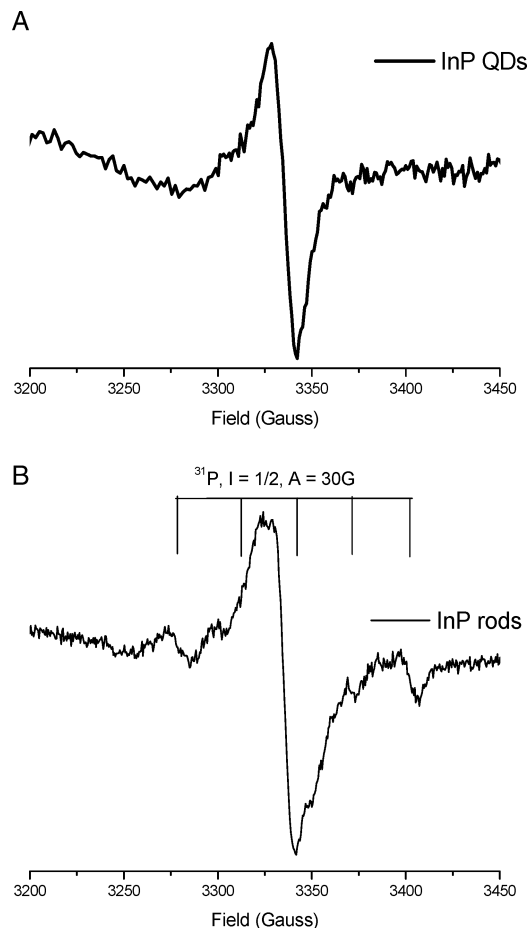


**Figure 2.** EPR spectra of (a) InP QDs (diameter  $4.7 \pm 0.5$  nm), and (b) QRs ( $6 \times 13$  nm) obtained upon excitation with white light ( $\lambda = 450$  nm) at 4.2 K. The EPR frequency is 9.345 GHz, MA is 6.3 G, time constant is 1.28 ms, and microwave power is 2 mW. The bars indicate hyperfine quintet that would be obtained due to the interaction of unpaired electron with four neighboring phosphorus atoms <sup>31</sup>P ( $I = 1/2$ , 100% natural abundance) with hyperfine coupling of  $A = 32$  G in zinc blende crystalline structure either at an In vacancy site or at an interstitial site ( $g = 2.001$ ).

particle, two paramagnetic species were observed that exhibited EPR signals at  $g = 2.055$  and  $g = 2.001$ . When the light was turned off, the signal at  $g = 2.001$  immediately disappeared at 8 K, while the signal at  $g = 2.055$  disappeared only slowly and could still be detected, even upon heating to room temperature. Our previous analysis<sup>22</sup> showed that the signal at  $g = 2.055$  was caused by trapped electrons located on the surface, while the signal at  $g = 2.001$  arose from delocalized holes in the QD core.

In rod-shaped nanocrystals (Figure 2b), slightly different paramagnetic species are formed during illumination compared to spherical InP nanocrystals. The difference arises due to different defect chemistry arising from the different synthetic approaches used for the preparation of the QDs and QRs. Dots are prepared in excess of indium (In/P = 1.5–2), while rods are prepared in a large excess of phosphorus (P/In = 20–30). The same signal at  $g = 2.001$  (delocalized hole) arises for rods and dots, while the signal at  $g = 2.055$  (electron adduct on the surface) is not formed in the rod sample. Instead, a new quintet spectrum indicative of hyperfine interaction with nuclear spin appears in the rod samples. Due to the absence of higher-order spin effects,<sup>24</sup> the splitting is believed to be caused by nuclear spin  $1/2$ , with an isotropic  $g$  value of 2.004. Because phosphorus <sup>31</sup>P has an  $I = 1/2$  nucleus with 100% abundance, it is apparent



that the spectrum arises from a radical interacting with four phosphorus atoms. Indium atoms, which are coordinated with four phosphorus atoms in the zinc blende structure, have a nuclear spin of  $I = 9/2$  and a large magnetic moment. Therefore, if a radical were centered at In atoms, a ten-line spectrum with large hyperfine coupling would be observed, as unpaired electrons would reside in the 5s orbitals of In. We have looked for the paramagnetic signature of this radical in a broad magnetic field range (500–12000 G) and did not observe additional lines indicative of an In-centered radical, suggesting that In is not participating in radical interactions. Therefore, we propose that acceptor states arising from In vacancies are formed in the QRs; these defect states are positively charged in the dark (empty of electrons) to maintain charge neutrality and do not become ionized because the ionization energy for creating holes in the valence band from this acceptor state is relatively large (about 200 meV for QDs<sup>22</sup>). However, under illumination, the In vacancy acceptor states become populated with electrons trapped from the conduction band and free holes are formed in the valence band. These holes produce the EPR signal at  $g = 2.001$ , while the electrons trapped in the In vacancy state produce the quintet spectrum.

Different EPR spectra were observed for Au/InP QR composites. To prepare Au/InP QR composites, we employ gold nanoparticles to catalyze and direct one-dimensional rod growth in solution. The procedure used is the same as that used by Banin et al.<sup>6</sup> for the synthesis of InAs and InP QRs with  $\sim 2$ -nm Au nanoparticles. Figure 3 shows TEM images and the absorption spectrum of Au/InP QRs with a short length obtained after size-selective precipitation. The quantum rods have a mean diameter of 4 nm and varying length of 12–20 nm. Z-analysis of TEM images (bright images, Figure 3b) shows that the Au particles are not attached at the rod tip but are located inside the InP nanorods, close to the rod tip.

Photoinduced EPR signals of electron and hole adducts obtained for Au/InP QRs are presented in Figure 4 and compared to the EPR signals observed in pure 2-nm Au particles. EPR spectra in Figure 4 are obtained under the same conditions as those for pure InP QRs and QDs in Figure 3. Comparison of the EPR signals for Au and Au/InP QRs shows that both spectra are composed of two components: one a multiline spectrum with different hyperfine coupling and a narrow singlet center line. The multiline spectrum is reminiscent of the oxidized gold cluster  $\text{Au}_2^{2+}$  in which gold ions are associated with metallic Au atoms.<sup>21</sup> In this species, unpaired electrons of gold ions interact with two gold nuclei, which have nuclear spin of  $3/2$  and 100% natural abundance, resulting in a seven-line spectrum ( $g = 2.007$ ). The hyperfine splitting of 15 G measured in isolated Au nanoparticles is three times smaller than the one of free  $\text{Au}_2^{2+}$  clusters<sup>21</sup> and is in agreement with shared spin density within  $\text{Au}_2^{2+}$  clusters. An even smaller hyperfine splitting was measured in the samples in which gold particles are associated with InP QRs, indicating the electron density of these clusters is perturbed by the presence of InP; that in turn suggests that the interface between Au particles and InP rods is the place of localization of photogenerated holes. The central singlet line has the same width and the same  $g = 2.006$  for both Au/InP QRs and Au particles. While the shape of the signal is indicative of CESR (conduction electron spin resonance), the small  $g$  shift with respect to the value of the free electron resonance suggests trapped electrons exist at the Au nanoparticle surface site.

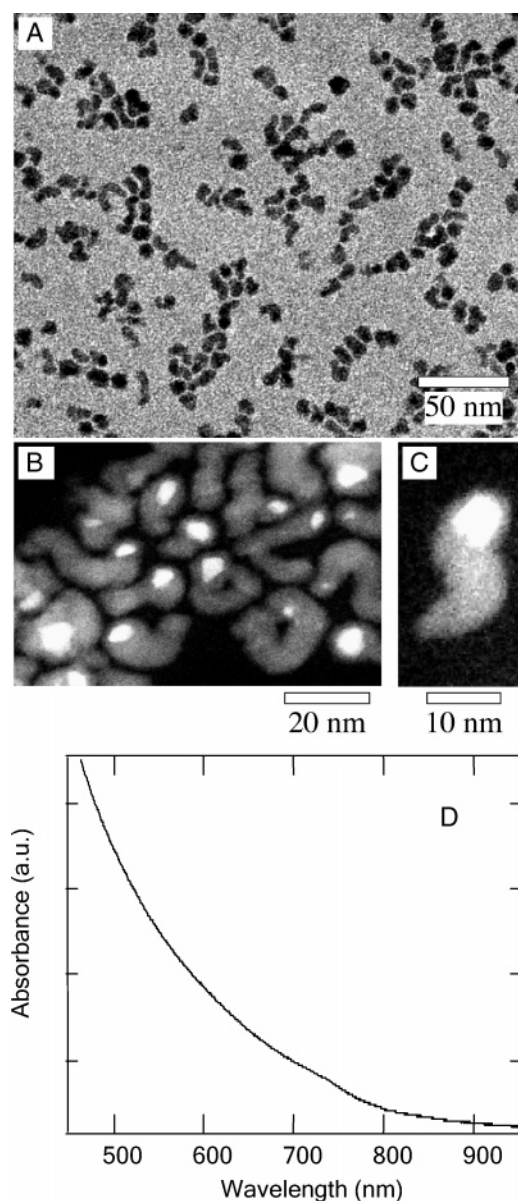


**Figure 3.** TEM images (a–c) and absorption spectrum (d) of the first fraction of InP QRs synthesized by SLS mechanism with 2-nm Au nanoparticles. (a) An ensemble of rods where many rods are kinked. (b, c) High-resolution images where gold particles can be identified on the rods as a bright image located inside QRs. (d) Absorption spectra of Au/InP rods.

The signal for electron trapping sites at  $g = 2.006$  is not the same as the signals present in either the metal-free InP dots or rods. This signal is connected with the new location of electrons in the presence of Au particles in InP QRs. During illumination, only the InP part of Au/InP QRs is photoexcited because the absorption coefficient of InP nanocrystals is larger than that of the surface plasmon resonance band in the absorption spectrum of 2-nm Au particles.<sup>25</sup> The contribution of the surface plasmon band at 520 nm cannot be seen in the absorption spectrum of Au/InP rods (Figure 3d).

Photogenerated electrons can be transferred from InP to Au nanoparticles in a Au/InP nanojunction. This transfer is thermodynamically favorable because in aqueous solution the Fermi level of Au is 0.45 V<sup>10</sup> versus NHE at pH 7, while bulk InP has a conduction band potential of  $-0.6$  V versus NHE at pH 7. For quantum rods, the conduction electron level will shift to even more negative values due to size quantization effects. The transfer of electrons from InP to Au continues until the two

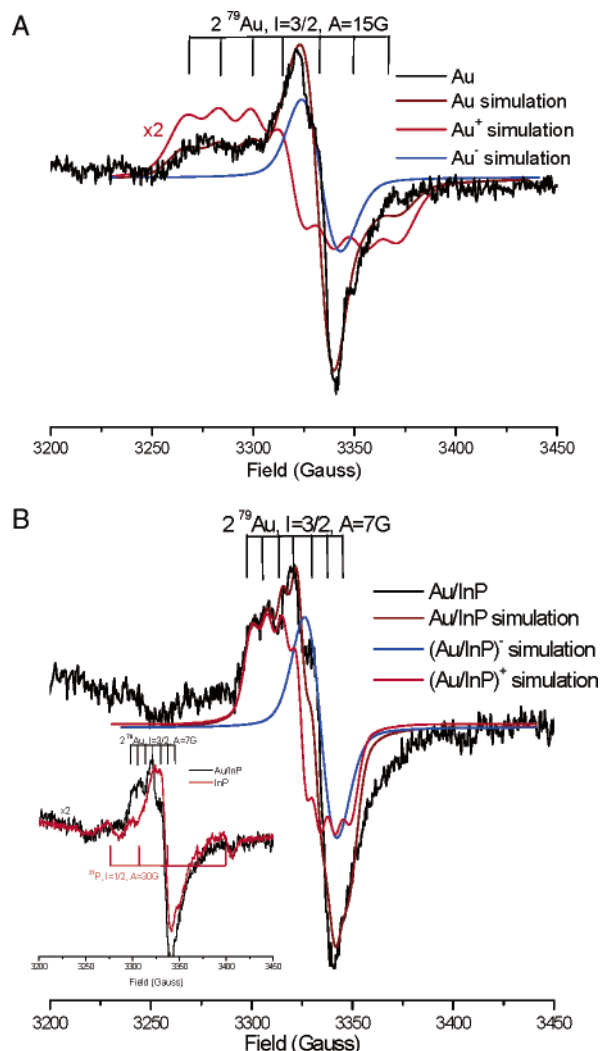


**Figure 4.** (a) EPR spectra of 2-nm Au nanoparticles, and (b) of Au/InP QR composite ( $4 \times 15$  nm) obtained upon laser excitation at 450 nm (15 mJ/pulse) and at 4.2 K. The EPR frequency is 9.345 GHz, MA is 6.3 G, time constant is 1.28 ms, and microwave power is 2 mW. The spectra were deconvoluted into a sum of two radical species using the Simfonia (Bruker) simulation program. The 0.5 Lorentzian/Gaussian line width of 17 G (a) and 8 G (b) and  $g$  tensors of 2.023 (a) and 2.020 (b) were used for simulation of  $(\text{Au})_n^+$  radical species, while 17 G (a) and 10 G (b) and  $g$  tensor of 2.0025 were used for an electron adduct radical species of  $(\text{Au})_n^-$ . The bars indicate hyperfine septet obtained for  $(\text{Au})_n^+$  radical species due to the interaction of unpaired electrons with two gold atoms  $^{197}\text{Au}$  ( $I = 3/2$ , 100% natural abundance) with (a) hyperfine coupling of  $A = 16$  G and (b)  $A = 7.5$  G, indicating different electron density of bare and InP coupled gold nanoparticles. The inset shows comparison between EPR spectra obtained by illumination of InP (Figure 2b) and Au/InP QRs. The difference is produced by the presence of metal and not by size or shape differences.

systems attain equilibration and the Fermi levels of the two phases become equal. As a result of charge equilibration between semiconductor and the metal nanoparticles, excess electrons accumulate in the Au particles and we can expect to see the EPR signal as shown in Figure 4b.

Our EPR results undoubtedly show that the electron in Au/InP QRs does not feel the change of electron density of InP, and it means that the electron is far from the InP part. The electron and the hole are located in the vicinity of the Au particles but in different places. Although the EPR study shows that the carrier charges are in different places in the Au/InP QRs, we can see very weak band edge emission in our Au/InP

QR sample that corresponds to the InP part. The electron transfer from the InP part to the Au particles competes with recombination of the electron–hole pair in the InP part of the rod, and a weak band edge can be seen. The EPR signal for excitons that form in the InP part during the absorption of light and recombined to yield emission cannot be seen because EPR can detect only paramagnetic species that reach a steady-state concentration of  $\sim 4 \times 10^{12}$  spins per  $\text{cm}^3$  at 10 K for a 20-G-wide signal.

## 2. Absorption and PL Spectra of $\text{In}^0/\text{InP}$ QD Composite.

We also studied the heterostructure of spherical InP QDs with indium particles.  $\text{In}^0$  particles are grown on InP QD surfaces that were initially passivated with oleic acid (3.5 nm in diameter) or with TOPO/TOP stabilizer (4.8 nm in diameter). The 3.5-nm InP QDs stabilized with oleic acid are shown in Figure 5a. A metallic indium island is grown on the QD surface by spontaneous decomposition of  $\text{C}_5\text{H}_5\text{In}$  in a toluene solution at 50 °C. A  $\text{C}_5\text{H}_5\text{In}$  solution was added very slowly over a period of 2 h to allow  $\text{In}^0$  nucleation on the InP surface. Indium grown on the surface of QDs is clearly identified by TEM (Figure 5b) as a point with enhanced contrast due to the higher electron-scattering cross section of indium compared to InP QDs. TEM images (Figure 5) show that metallic indium forms islands of irregular shape, which do not completely cover all the InP nanocrystals. We used the same molar concentration of  $\text{In}^0$  and InP QDs, which means that the volume of  $\text{In}^0$  particles that are formed should be smaller than that of InP QDs because of the difference in density between indium ( $7.3 \text{ g cm}^{-3}$ ) and InP ( $4.8 \text{ g cm}^{-3}$ ).

In addition to  $\text{In}^0/\text{InP}$  QD characterization with TEM, optical absorption measurements have been used to characterize the coupling of  $\text{In}^0$  and InP QDs. Figure 5c shows the evolution of the absorption spectra of 3.5-nm InP QDs after growth of metallic indium on the QD surface. The band edge peak of InP QDs, which is at 590 nm (2.1 eV), is red-shifted after growth of metallic indium (Figure 5c, curve 1). A red-shift of 50 and 70 meV in the  $\text{In}^0/\text{InP}$  QD composite is observed immediately upon the measurement (Figure 5c, curve 2) and after aging of the sample for two weeks (Figure 5c, curve 3), respectively. Absorption of light by  $\text{In}^0$  above 400-nm wavelength does not interfere with the absorption spectrum of InP QRs because the plasmon surface band is at 240 nm.<sup>26</sup> The changes of the position of the first exciton by addition of indium on the surface can be attributed to the delocalization of the electron over the whole  $\text{In}^0/\text{InP}$  composite and also to the change of polarization energy of the exciton due to the increase of the dielectric constant of the shell around InP in the presence of the  $\text{In}^0$  island. The Coulomb attraction energy will decrease only slightly due to the asymmetry of  $\text{In}^0$  growth on InP QDs. Figure 5c, curve 4, shows that annealing at 180 °C for a half hour increased the width at the peak of the first exciton and also affected its position by a red-shift of about 160 mV. Melted indium (mp 157 °C) at 180 °C is spread better on the QD surface after annealing, and that improves the contact between the  $\text{In}^0$  droplets and InP QDs. At 180 °C, the particles do not aggregate; they are soluble in nonpolar solution, and TEM analysis shows that most  $\text{In}^0/\text{InP}$  particles are individual dots of about 3.5–5.0-nm diameter (Figure 5c). When strong contact between InP and In is reached, then strong mixing of the semiconductor and metal electronic states can occur that exhibit broadened levels and reduced band gap (Figure 5c, curve 4). Similar results were observed by loading  $\text{In}^0$  on 4.8-nm InP QDs that were capped with TOPO/TOP.

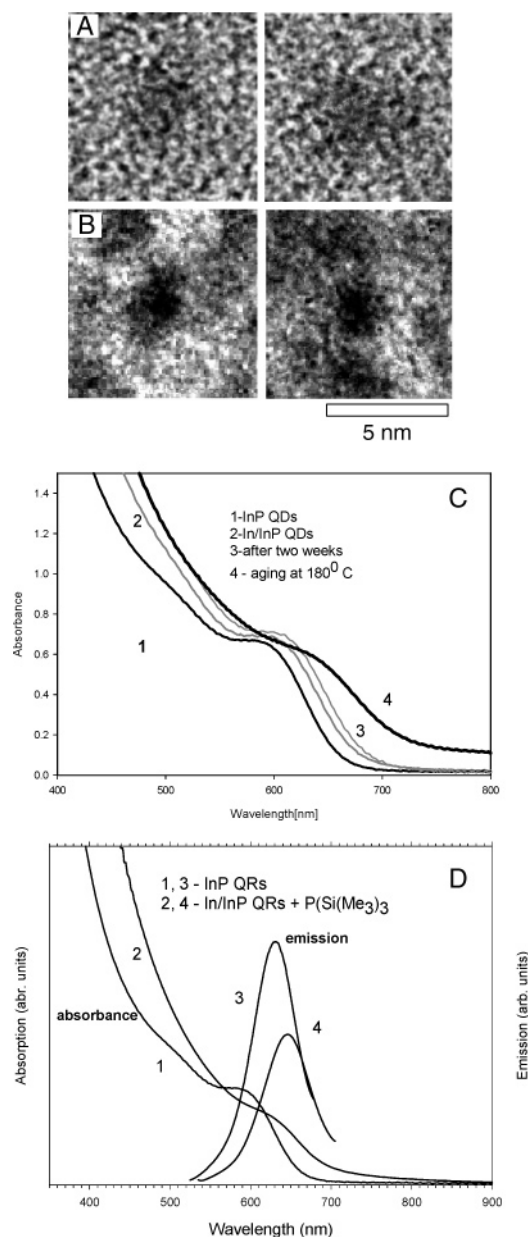


**Figure 5.** (a) TEM images showing a high-resolution TEM micrograph of individual, spherical 3.5-nm InP QDs. (b) In/InP QDs after annealing at 180 °C. (c) Absorption spectra of 3.5-nm InP QDs (curve 1) and after deposition of In<sup>0</sup>: immediately (curve 2), after two weeks (curve 3), and after heating at 180 °C (curve 4). (d) Absorption and emission spectra of pure InP QDs (curves 1, 3), and after addition of In<sup>0</sup> droplet (the sample is the same as that in Figure 5a, curve 4) and exposure to P(SiMe<sub>3</sub>)<sub>3</sub> and heated at 260 °C for two hours (curves 3, 4, respectively).

The emission is partially quenched after addition of metallic indium on the surface and completely quenched after annealing at 180 °C. The mechanism responsible for quenching of PL can be explained by electron tunneling from electron–hole pairs in the InP, followed by electron capture in indium particles and nonradiative recombination with holes in the InP core. Energy transfer from photoexcited InP particles to In<sup>0</sup> particles does not occur because the surface plasmon band for In<sup>0</sup> particles is at higher energy (240 nm) than that of the first exciton energy of InP QDs. Our results are in agreement with recently published results of Banin et al.<sup>13</sup> that showed when gold tips are grown on CdSe nanorods, a change of optical properties of the nanorods occurs that is caused by strong coupling between the gold and semiconductor parts, and that emission is quenched by the gold

tip via a new nonradiative pathway. The emission of In<sup>0</sup>/InP QD composites annealed at 180 °C can be recovered when metallic indium is converted into InP by reaction with P(SiMe<sub>3</sub>)<sub>3</sub>. The absorption spectrum is slightly shifted to the red with a long tail (Figure 5d, curve 2), indicating the broad size distribution of InP QRs as the emission spectrum is recovered (Figure 5d, curve 4). This experiment also confirms that strong PL quenching in the In<sup>0</sup>/InP composite is a consequence of the presence of In<sup>0</sup> on the nanocrystal surface because when In<sup>0</sup> is removed by reaction with P(SiMe<sub>3</sub>)<sub>3</sub>, emission again appears.

In conclusion, we have demonstrated that heterostructures of semiconductor and metal particles improve the photoinduced charge-transfer efficiency. The interaction of metal with semiconductor nanocrystals provides new functionalities to the nanostructures and the possibility of charge separation. EPR studies show that charge separation occurs in elongated semiconductor quantum rods that grow on metallic catalysts and that the electron and the hole are located in the vicinity of metal particles but at completely different places. The results elucidate the difference in the electronic properties of elongated semiconductors that grow on metallic catalysts compared to pure semiconductor nanocrystals of the same shape. When melted indium particles are grown on the surface of colloidal spherical InP nanocrystals (In<sup>0</sup>/InP QDs), the optical properties change and the band gap moves to lower energy due to the strong mixing of the semiconductor and metal electronic states while emission is completely quenched.

Our study shows that the presence of metal as an incorporated part of the semiconductor quantum structures such as dots and rods produces large changes in their electronic properties. Soon, we plan to study the conductivity of this heterostructure using time-resolved terahertz spectroscopy and ultrafast electron dynamics to distinguish differences in electronic structure between metal–semiconductor and metal-free semiconductor nanocrystals. This study will help in understanding this class of materials and their possible use in optoelectronic applications such as solar cells.

**Acknowledgment.** The work at ANL (Contract No. W-31-109-ENG-38) and NREL was supported by the U.S. Department of Energy, Office of Science, Office of Basic Energy Sciences, Division of Chemical Sciences, Geosciences and Biosciences. Use of John Cowley Center for High Resolution Microscopy is gratefully acknowledged, and we thank Renu Sharma for assistance with TEM HRTEM investigations.

## References and Notes

- (1) Ellingson, R. J.; Blackburn, J. L.; Nedeljković, J. M.; Rumbles, G.; Jones, M.; Fu, H.; Nozik, A. J. *Phys. Rev. B* **2003**, *67*, 075308.
- (2) Shabaev, A.; Efros, A. L. *Nano Lett.* **2004**, *4*, 1821.
- (3) Muljarov, E. A.; Zhukov, E. A.; Dneprovskii, V. S.; Masumoto, Y. *Phys. Rev. B* **2000**, *62*, 7420.
- (4) Trentler, T. J.; Goel, S. C.; Hickman, K. M.; Viano, A. M.; Chiang, M. Y.; Beatty, A. M.; Gibbons, P. C.; Buhro, W. E. *J. Am. Chem. Soc.* **1997**, *119*, 2172.
- (5) Lieber, C. M. *Solid State Commun.* **1998**, *107*, 607.
- (6) Kan, S.; Mokari, T.; Rothenberg, E.; Banin, U. *Nat. Mater.* **2003**, *2*, 155.
- (7) Yu, H.; Li, J.; Loomis, R. A.; Wang, L.-W.; Buhro, W. E. *Nat. Mater.* **2003**, *2*, 517.
- (8) Ahrenkiel, S. P.; Mičić, O. I.; Miedaner, A.; Curtis, C. J.; Nedeljković, J. M.; Nozik, A. J. *Nano Lett.* **2003**, *3*, 833.
- (9) Wood, A.; Giersig, M.; Mulvaney, P. J. *Phys. Chem. B* **2001**, *105*, 8810.
- (10) Jakob, M.; Levanon, H.; Kamat, P. V. *Nano Lett.* **2003**, *3*, 353.
- (11) Shimizu, K. T.; Woo, W. K.; Fisher, B. R.; Eisler, H. J.; Bawendi, M. G. *Phys. Rev. Lett.* **2002**, *89*, 117401.
- (12) Kulakovich, O.; Strekal, N.; Yaroshevich, A.; Maskevich, S.; Gaponenko, S.; Nabiev, I.; Woggon, U.; Artemyev, M. *Nano Lett.* **2002**, *2*, 1449.



- (13) Mokari, T.; Rothenberg, E.; Popov, I.; Costi, R.; Banin, U. *Science* **2004**, *304*, 1787.
- (14) Nedeljković, J. M.; Mičić, O. I.; Ahrenkiel, S. P.; Miedaner, A.; Nozik, A. J. *J. Am. Chem. Soc.* **2004**, *126*, 2632.
- (15) Brust, M.; Walker, M.; Bethell, D.; Schiffrin, D. J.; Whyman, R. *J. Chem. Soc., Chem. Commun.* **1994**, 801.
- (16) Mičić, O. I.; Jones, K. M.; Cahill, A.; Nozik, A. J. *J. Phys. Chem. B* **1998**, *102*, 9791.
- (17) Battaglia, D.; Peng, X. *Nano Lett.* **2002**, *2*, 1027.
- (18) Rosenthal, J.; Yarmus, L. *Rev. Sci. Instrum.* **1966**, *37*, 381.
- (19) Rajh, T.; Ostafin, A. E.; Mičić, O. I.; Tiede, D. M.; Thurnauer, M. C. *J. Phys. Chem.* **1996**, *100*, 4538.
- (20) Halperin, W. P. *Rev. Mod. Phys.* **1986**, *58*, 533.
- (21) Claus, P.; Brückner, A.; Mohr, C.; Hofmeister, H. *J. Am. Chem. Soc.* **2000**, *122*, 11430.
- (22) Mičić, O. I.; Nozik, A. J.; Lifshitz, E.; Rajh, T.; Poluektov, O. G.; Thurnauer, M. C. *J. Phys. Chem. B* **2002**, *106*, 4390.
- (23) Langof, L.; Ehrenfreund, E.; Lifshitz, E.; Mičić, O. I.; Nozik, A. J. *J. Phys. Chem. B* **2002**, *106*, 1606.
- (24) Kennedy, T. A.; Wilsey, N. D.; Krebs, J. J.; Stauss, G. H. *Phys. Rev. Lett.* **1983**, *50*, 1281.
- (25) Palpant, B.; Prével, B.; Lermé, J.; Cottancin, E.; Pellarin, M.; Treilleux, M.; Perez, A.; Vialle, J. L.; Broyer, M. *Phys. Rev. B* **1998**, *57*, 1963.
- (26) Zhao, Y.; Zhang, Z.; Dang, H. *J. Phys. Chem.* **2003**, *107*, 7574.